Optimization of the Inlet and Outlet Structure of a Motorcycle Thermoelectric Generator to Reduce Pressure Drop

Thong Duc Hong[1,2,*], Minh Quang Pham[1,2], An Vu Cao[1,2], Kha Nguyen Tran[1,2], Son Thanh Tran[1,2], Thang Viet Vu[1,2]

[1]Faculty of Transportation Engineering, Ho Chi Minh City University of Technology (HCMUT), Ho Chi Minh City, 700000, Vietnam, email: hongducthong@hcmut.edu.vn; pqminh.sdh2412@hcmut.edu.vn; an.cao193@hcmut.edu.vn; kha.tran2111435@hcmut.edu.vn; son.tran2112204@hcmut.edu.vn; thang_vv@hcmut.edu.vn

[2]Vietnam National University Ho Chi Minh City (VNU-HCM), Ho Chi Minh City, 700000, Vietnam.
*Corresponding Author: hongducthong@hcmut.edu.vn

Abstract: This study presents an optimal design process for the muffler geometry to reduce the pressure drop of a motorcycle thermoelectric generator system by applying elliptical and contraction profiles. The elliptical profile is used at the junction between the front wall of the muffler and the inlet pipe as well as between the outlet pipe and the rear wall, with optimized semi-major axes, b and e, respectively. Two profiles are applied and compared at the junction between the front wall and muffler body, containing an elliptical profile with optimal semi-major axis, c, and contraction with optimal polynomial order, P_i. Finally, the contraction profiles are selected to be used at the junction between the rear wall and the muffler body, P_o. The results reveal that these profiles reduce the impact of sudden cross-sectional changes and diminish vortex formation, thus decreasing local pressure drop at the applied locations and contributing significantly to the overall pressure drop reduction of the thermoelectric generator system. Besides, the effects of optimal elliptical profiles at the inlet and outlet are more substantial than those of the optimal contraction profiles at the muffler body. The optimal parameters, b = 20mm, third-order polynomial P_i, e = 20mm, fifth-order polynomial P_o, reduce pressure drop by 43% compared to the original and nearly 8% compared to the previous. This study contributes an optimal design process to reduce pressure drop for motorcycle thermoelectric generator systems by practically applying high-efficiency aerodynamic profiles, thereby providing a foundation for designing, manufacturing, and commercializing the system.

Keywords: Thermoelectric generator; pressure drop; muffler structure; elliptical profile; contraction profile

1 Introduction

The global community has serious concerns about resource shortages, fuel depletion, and environmental pollution, worsened by the increase in vehicle production. For traditional internal combustion engine vehicles, the efficiency is limited to approximately 30%, with approximately 40% of the input energy being lost directly through the exhaust system [1]. Consequently, vehicle waste heat recovery has become a highly compelling topic, particularly in the automotive industry. In this context, thermoelectric generators (TEG) have shown promise in capturing exhaust heat and directly converting it into electrical energy [2]. TEGs are environmentally friendly, compact, and well-suited to small-scale applications. Moreover, they quietly operate without moving mechanical components, eliminating maintenance and replacement costs [3].

Enhancing the efficiency of thermoelectric generator systems (TGS) has been examined in several studies. The allocation of the heat exchanger area was optimized to improve power efficiency by Tian et al. [4]. The findings revealed that expanding the total heat exchange area from 0.03 m^2 to 0.09 m^2 significantly boosted maximum power output from 0.02 W to 0.26 W, increasing the optimal output current by 138 %. Hong et al. [5] investigated the impact of guide fin structures on the temperature uniformity of TGS. The results demonstrated a significant enhancement in temperature uniformity, with a reduction of 93.9 % in cross-sectional temperature difference. He et al. [6] used 50 mm × 50 mm thermoelectric modules (TEMs) for comparison and discovered that the output power of the optimal hybrid electric structure outperformed the series and parallel configurations by 7.16 % and 7.34 %, respectively. Yang et al. [7] integrated a TGS with a three-way catalytic converter, achieving simultaneous improvements in output power and reductions in exhaust system pressure loss. Hong et al. [8,9] optimized the placement and structure of guide fins inside the muffler inlet compartment. The results indicated that the double-layer guide fin structure significantly enhanced both exhaust gas flow uniformity and heat exchange capacity compared to the single-layer configuration. A multi-objective optimization of the heat sink and heat pipes of the TGS under natural convection was conducted by Elghool et al. [10]. According to the analysis of variance results, the influence of geometric parameters on power output and efficiency of TGS was ranked as the following order: fin height > fin length > fin spacing. Hong et al. [11] optimized the outlet pipe structure, resulting in a 50% improvement in temperature uniformity. Luo et al. [12] optimized the exhaust channel of the automobile thermoelectric generator. The results revealed that the distance and thickness of the fins were 2 mm and 0.5 mm, respectively, producing the maximum net power and net efficiency. Chen et al. [13] evaluated the exhaust heat recovery capabilities of a low-temperature TGS with plate fins. The findings showed that, with a Reynolds number of 1000, installing nine fins enhances mean conversion efficiency and total output power of TGS by 35 % and 85 % compared with a configuration without

fins, respectively. Hong et al. [14] further optimized the original rectangular fin profile into an optimal parabolic profile for the hot-side heat exchanger to achieve temperature consistency of the TGS along the exhaust flow.

Although integration of the TGS into the muffler makes the system more compact and improves its efficiency, an increase in pressure drop is introduced owing to rapid flow expansion, frictional losses, and abrupt velocity changes [15], which result in higher exhaust pressures, reduced intake efficiency, and other detrimental effects [16]. Significant pressure drop indicates ineffective discharge of engine exhaust gas from the heat exchanger, causing back pressure that reduces engine longevity and efficiency [17]. Therefore, enhancing heat transfer efficiency while controlling the pressure loss of the system is crucial for developing TGS [18]. Kim et al. [19] demonstrated that the pressure drop grows proportionally as the fin thickness and quantity increase. Wang et al. [20] replaced the finned structure with a concave design on the hot-side heat exchanger of the automotive TGS, reducing pressure drop by 20.57% compared to the finned configuration. Kim et al. [21] found that the pressure drop occurs mostly at connection zones due to the abrupt changes in the exhaust stream orientation, accounting for around 63%-84% of the overall pressure drop. The literature review shows that various interior configurations for heat exchangers and mufflers have been proposed that might improve efficiency while decreasing pressure drop. Pressure reduction can be improved substantially by modifying the structural design of the muffler inlet and outlet, yet this approach has received limited attention.

In previous studies by the authors [5,8,9,11], the temperature distribution on the transverse section of the TGS was improved by enhancing exhaust-gas-flow uniformity. Then, the performance of the TGS was subsequently increased by optimization of plate-fin parameters [22]. These efforts addressed the issues of temperature uniformity and thermal-power optimization; however, as previously mentioned, when a finned heat collector is incorporated into the muffler, the primary cause of pressure drop originates from the exhaust pipe configuration [21]. Thus, the most common profiles, i.e., circular and chamfered profiles, were employed to diminish the pressure drop of TGS [23]. Consequently, a significant reduction in pressure drop was obtained since these profiles mitigated the vena-contracta effect and suppressed vortex formation. Nevertheless, pressure drop could be further improved by using highly efficient aerodynamic profiles.

In this study, the authors seek to eliminate the pressure drop of the TGS by using high-efficiency aerodynamic profiles. The first one is the elliptical profile, which is expected to outperform the circular profile, and the other one is the contraction profile, researched and applied by Bell and Mehta [24] for small and low-speed wind tunnels. These profiles are implemented at the inlet and outlet parts of the muffler, and their parameters are optimized to minimize the pressure drop through a series of computational fluid dynamics (CFD) simulations.

The primary objective of this study is to offer a practical design methodology for minimizing pressure drop in the motorcycle exhaust TGS using highly efficient aerodynamic profiles, thereby seeking to boost the commercialization potential of thermoelectric generators and enhance their practical viability.

2 Materials and Methods

2.1 Structural Description of TGS Integrated with the Muffler of the Motorcycle

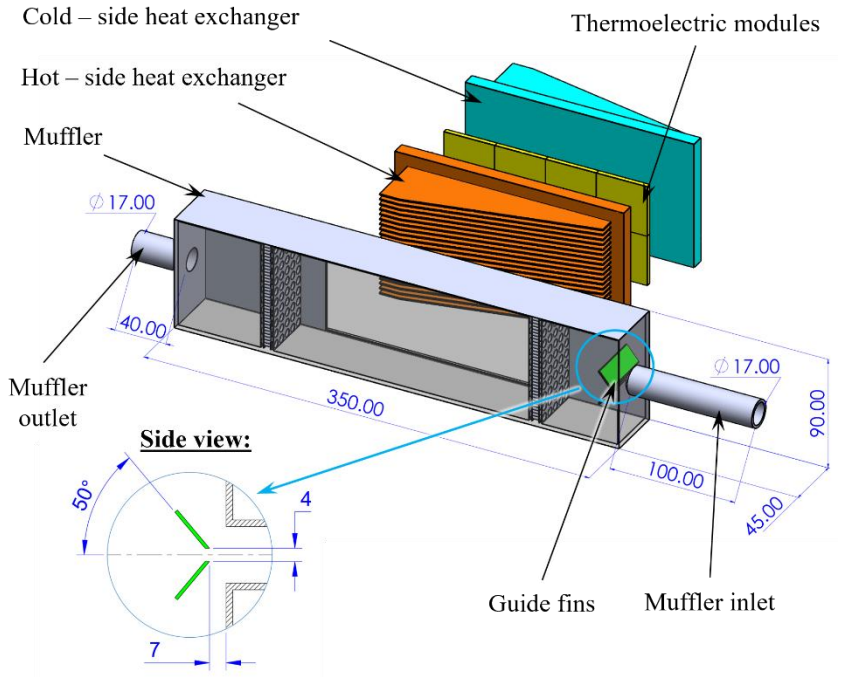

Figure 1
The structure of the TGS.

The configuration of the TGS is shown in Figure 1, consisting of a muffler, thermoelectric modules, a hot-side heat exchanger, and a cold-side heat exchanger. The muffler with a rectangular cross-section replaces the original muffler of the motorcycle. It is divided into three parts: the inlet part with an inlet pipe and guide fins, the middle part providing a location for installing the hot-side heat exchanger, and the outlet part with a hollow chamber and an outlet pipe. The overall dimensions of the muffler body are 410x90x45 mm in LxHxW, and the inlet and outlet

diameters are 17 mm. Thermoelectric modules are sandwiched between the two heat exchangers, with additional plate fins to enhance heat transfer from the exhaust. The hot-side heat exchanger is integrated with the middle part of the muffler to absorb heat from the exhaust gas, and the cold-side heat exchanger is used to dissipate the transferred heat directly to the ambient air.

In this work, the inlet and outlet parts of the muffler were optimized according to the flowchart presented in Figure 2. Five parameters were investigated, including the semi-major axis length of the elliptical profile, b, connecting the front wall of the muffler and inlet pipe; the polynomial order of the contraction profile, P_i, or the semi-major axis length of the elliptical profile, c, connecting the front wall and muffler body; the semi-major axis length of the elliptical profile, e, connecting the outlet pipe and the rear wall of the muffler; and the polynomial order of the contraction profile, P_o, between muffler body and rear wall. The optimization procedure contained four simulation series, conducted in the sequence as follows: firstly, b was changed in the range of 12 to 20 mm in 2 mm increments; secondly, the polynomial order P_i was sequentially set to the 3rd, 5th, and 7th orders, and c was varied from 20 to 60 mm in 20 mm increments, then after the optimal case was determined by comparing the results; thirdly, e was varied from 12 to 20 mm in 2 mm increments; finally, the polynomial order P_o was set to the 3rd, 5th, and 7th orders sequentially.

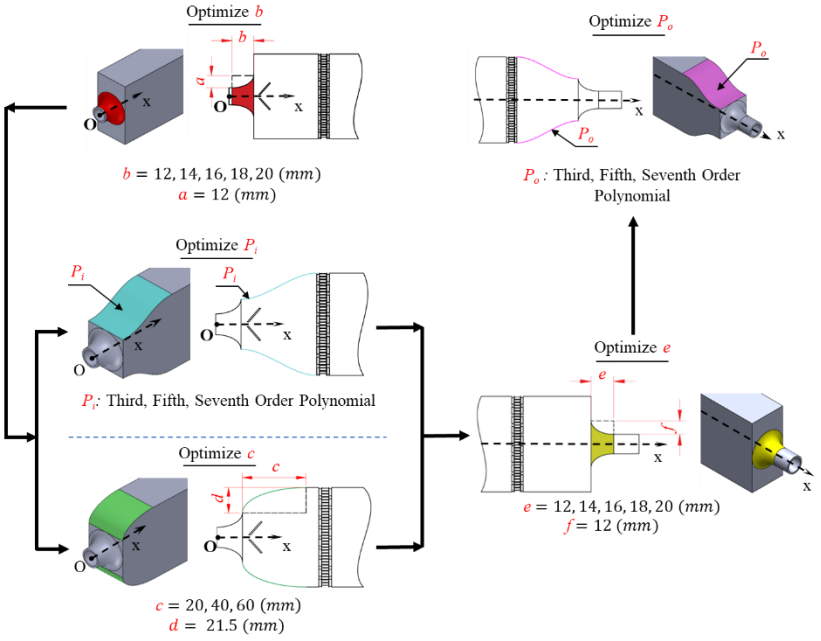

Figure 2
Process for optimizing the inlet and outlet structure of the muffler

For the aerodynamic contraction profile, the polynomial curves of different orders are illustrated in Figure 3 and determined as follows [22]:

Third order polynomial:

$$P_3 = H_i - (H_i - H_0)\left(-2\psi^3 + 3\psi^2\right) \tag{1}$$

Fifth order polynomial:

$$P_5 = H_i - (H_i - H_0)\left(6\psi^5 - 15\psi^4 + 10\psi^3\right) \tag{2}$$

Seventh order polynomial:

$$P_7 = H_i - (H_i - H_0)\left(-20\psi^7 + 70\psi^6 - 84\psi^5 + 35\psi^4\right) \tag{3}$$

where H_i, H_o, L are illustrated in Figure 3, $\psi = x/L$ where x is the abscissa of a point on the contraction profile, and L is the length of the contraction.

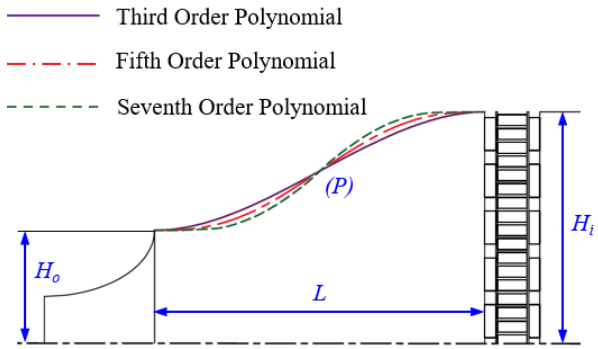

Figure 3
The fundamental dimensions of a contraction profile

2.2 CFD Simulation Description

2.2.1 Computational Model

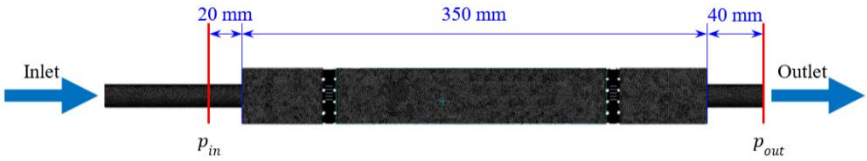

Figure 4
The CFD computational meshing model

The computational meshing of the CFD simulation developed in the previous study of the authors [21] is shown in Figure 4. Because the current research concentrates on the pressure drop caused by the muffler structure, the computational domain was limited to the exhaust gas inner side of the TGS, which was meshed with tetrahedral elements. After the mesh-independent test, the final mesh contained 5.3 million elements, with an overall element size of 1.2 mm and a curvature of 0.5 mm. Additionally, the inlet pipe of the model was extended to better match the actual geometry, while the exhaust inlet and outlet pressures were measured at the location shown in Figure 4.

2.2.2 Boundary Conditions

A Honda Wave 110 motorcycle was selected as the model for the TGS installation. The engine speed used in the simulation was 4925 rpm, corresponding to a vehicle speed of 50 km/h. The inlet temperature was 712 K, determined experimentally; whereas, the other physical properties, such as dynamic viscosity of 3.655×10^{-5} Ns/m^2 and density of 0.474 kg/m^3, were determined based on the exhaust gas temperature [8]. Engine speed and cylinder displacement were used to compute the exhaust gas flow rate, which was 4.02 l/s. The outlet pressure was set to be equivalent to the atmospheric pressure.

2.2.3 Governing Equations

In CFD simulation, the momentum and continuity equations have been used in the Cartesian coordinate system to describe the flow, as represented by the following formulas:

$$\operatorname{div}\left(\rho u_i \mathbf{u}\right) = -\frac{\partial p}{\partial x_i} + \mu \operatorname{div}\left(\operatorname{grad} u_i\right) \tag{4}$$

$$\operatorname{div}\left(\rho \mathbf{u}\right) = 0 \tag{5}$$

where $\mathbf{u}$ is the fluid velocity vector. u_i the velocity components according to the Cartesian coordinate system. μ, p, and ρ are the dynamic viscosity, the pressure, and the fluid density, correspondingly.

The turbulence was modeled by using the realizable k-ε model. This model is superior to the standard k-ε model, with more accurately arranged vortices. The equations for the model are expressed in the following formulas:

$$\operatorname{div}\left(k u_i\right) = \frac{1}{\rho} \operatorname{div}\left[\left(\mu + \frac{\mu_t}{\sigma_k}\right) \operatorname{grad} k\right] + \frac{G_k + G_b}{\rho} - \varepsilon \tag{6}$$

$$\operatorname{div}(\varepsilon u_i) = \frac{1}{\rho}\operatorname{div}\left[\left(\mu + \frac{\mu_t}{\sigma_\varepsilon}\right)\operatorname{grad}\varepsilon\right] + C_1 S\varepsilon - C_2\frac{\varepsilon^2}{k+\sqrt{v\varepsilon}} + C_{1\varepsilon}\frac{\varepsilon}{k}C_{3\varepsilon}G_b \tag{7}$$

$$v_t = C_\mu \frac{k^2}{\varepsilon} \tag{8}$$

where k is turbulence kinetic energy and ε represents turbulence energy dissipation rate. v is the kinetic viscosity. Specific descriptions of σ_k, G_k, G_b, σ_ε, $C_{1\varepsilon}$, C_2, $C_{3\varepsilon}$, S, and C_μ can be found in Ref. [23].

2.3 Pressure Drop and Pressure Power Loss

This study defines the pressure drop as the total pressure differential across the inlet and outlet of the muffler. It can be obtained by subtracting the pressure at the inlet plane from the pressure at the outlet plane, which are harvested from the CFD simulation:

$$\Delta p = p_{in} - p_{out} \tag{9}$$

where Δp presents the pressure drop of the system. p_{in} and p_{out} the total pressures at the inlet and outlet plane, which are indicated in Figure 4.

The pressure power loss is determined by using the following equations:

$$P_{loss} = Q\Delta p \tag{10}$$

(10)

where Q presents the exhaust flow rate.

3 Results and Discussions

3.1 Effect of the Length of the Semi-Major Axis of the Elliptical Profile, *b*

The variation of the pressure drop, Δp, as the exhaust gas passes through the TGS, with the semi-major axis length of the elliptical profile, b, ranging from 12 to 20 mm, is illustrated in Figure 5. The results indicate that when b increases, Δp decreases, reaching its lowest value of 141 Pa at b = 20 mm. This decrease is

attributed to the decline in abrupt cross-sectional changes when b grows, facilitating a reduction in losses within the inlet part of the muffler. Figure 6 illustrates the exhaust flow distribution within the inlet part for three configurations: (a) $b = 0$ mm, (b) $b = 12$ mm, (c) $b = 20$ mm. In the original configuration ($b = 0$ mm), the sharp corner between the front wall of the muffler and the inlet pipe causes flow separation [24,25], resulting in vortices and turbulence due to intense mixing at various points (see Figure 6a), which contribute to energy dissipation. With $b = 12$ mm, the rounded elliptical profile (effectively circular in this case) moderates the cross-sectional change along the exhaust flow path, allowing exhaust gas to expand gradually with reduced vortex formation [26] (see Figure 6b). In addition, since b rises, the distance from the corner of the inlet pipe to the guide fins becomes wider, leading to a reduction in local velocity at this location (see Figure 6c). Therefore, the Δp in this part decreases.

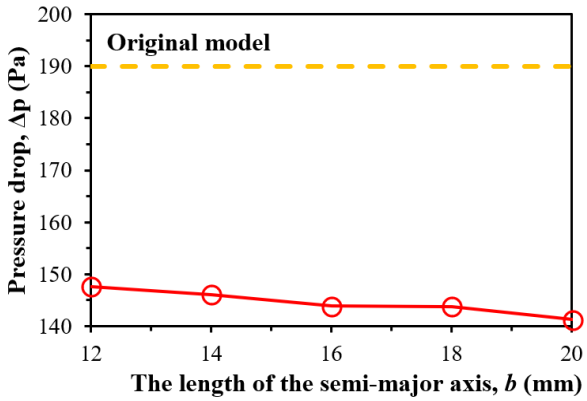

Figure 5

Pressure drop versus the semi-major axis length of the elliptical profile, b

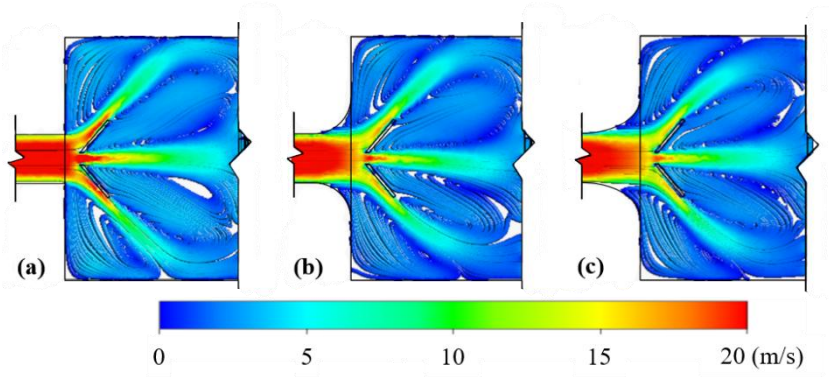

Figure 6

Exhaust flow distribution in the inlet part of the muffler for (a) $b = 0$ mm, (b) $b = 12$ mm, and (c) $b = 20$ mm

3.2 Effect of the Polynomial Order of the Contraction Profile, P_i and the Length of the Semi-Major Axis of the Elliptical Profile, c

Figures 7 and 8 show the variation of Δp when exhaust gas passes through the TGS as a function of the polynomial order of the contraction profile, P_i, and length of the semi-major axis, c, ranging from 0 to 60 mm, respectively. The results reveal that the third-order P_i is the optimal case, and then Δp increases gradually for the fifth- and seventh-order polynomials. By contrast, c does not exert a substantial effect on Δp. Although Δp generally decreases as c increases, Δp at c = 20 and 40 mm is higher than the previous; a slight reduction is observed at c = 60 mm but it is not substantial.

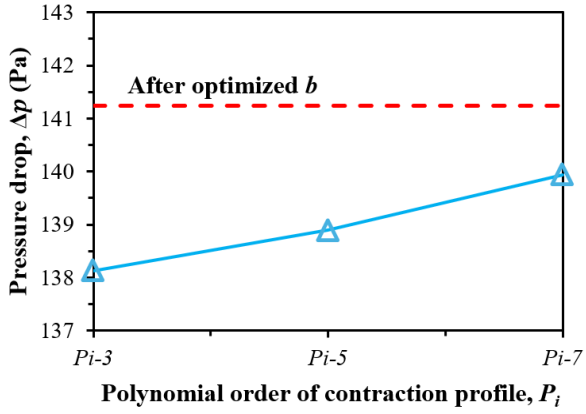

Figure 7
Pressure drop versus the polynomial order of the contraction profile, Pi

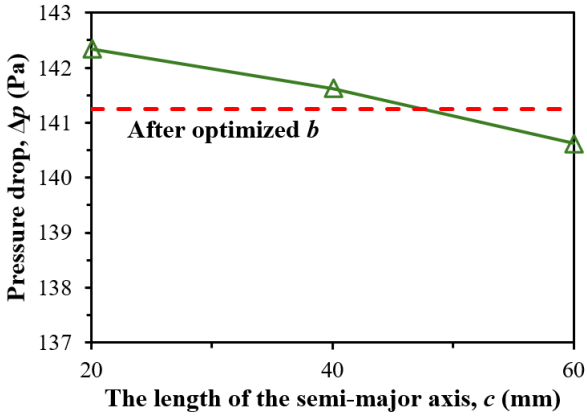

Figure 8
Pressure drop versus the major semi-axis length of the elliptical profile, c

Figure 9 shows the exhaust flow distribution within the inlet part of the model after optimizing b, c = 20, c = 60, P_i–3, P_i–5, and P_i–7. When c = 20 mm (see Figure 9b), its curvature makes the vortices in the region bounded by the guide fins and the walls of the muffler enlarge and obstruct the flow, leading to an increase in Δp. As c is increased to 40 and 60 mm, Δp gradually decreases due to the vortices, and reverse flows in this region are diminished (see Figure 9c). Therefore, when c increases to 60 mm, Δp tends to decrease, but it is not considerable compared to the previous value. In contrast, when applying the third-order contraction profile (P_i–3), the vortices are almost eliminated (see Figure 9d). When the higher-order contraction profiles are applied, the passage area between guide fins and the contraction profile becomes narrow, leading to an increase in the exhaust velocity and pressure drop (see Figures 9e and 9f).

Although it can be predicted that increasing the length c beyond 60 mm would further reduce pressure drop, it is impossible to increase c further due to the size limitations. Therefore, the optimal profile at this junction is the third-order contraction profile, P_i–3.

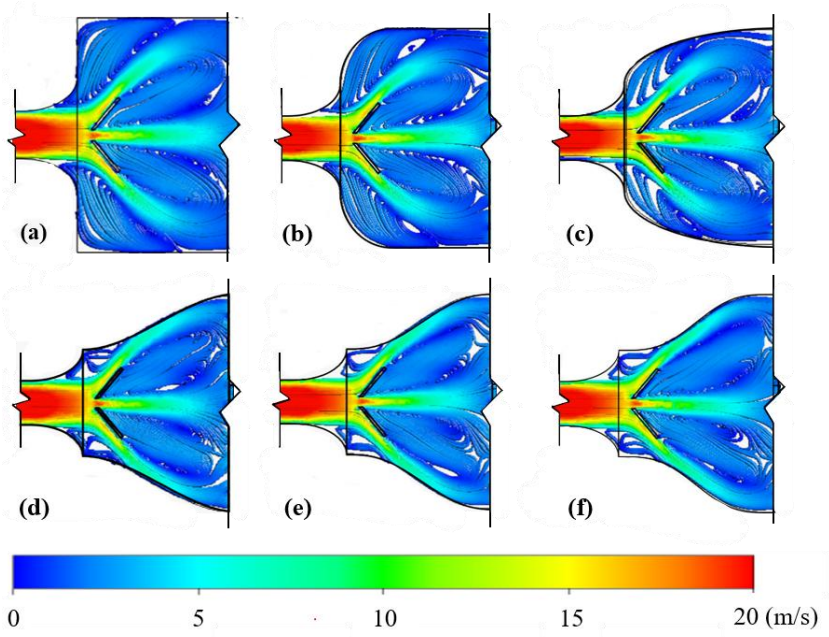

Figure 9

Exhaust flow distribution in the inlet part of the muffler for (a) After optimized b, (b) c = 20 mm, (c) c = 60 mm, (d) Pi–3, (e) Pi–5, (f) Pi–7

3.3 Effect of the Length of the Semi-Major Axis of the Elliptical Profile, *e*

Figure 10 shows the variation of Δp when exhaust gas passes through the TGS, with the length of the semi-major axis e ranging from 0 to 20 mm. The data indicate a significant decrease in pressure drop at e = 12 mm, followed by a more gradual decrease as e increases further. The minimum pressure drop of 104 Pa occurs at e = 20 mm. Figure 11 depicts the exhaust flow distribution in the outlet part of the model after optimizing P_i, e = 12 mm, and e = 20 mm. In Figure 11a, the sudden change in the cross-sectional area leads to the formation of a vena contracta [26], resulting in a significant local pressure drop. The impact of the vena contracta effect [26] is markedly diminished at e = 12 mm, corresponding to a rounded contour. As e increases, the variation of cross-sectional area along the output pipe decreases, yielding a further reduction in local pressure drop.

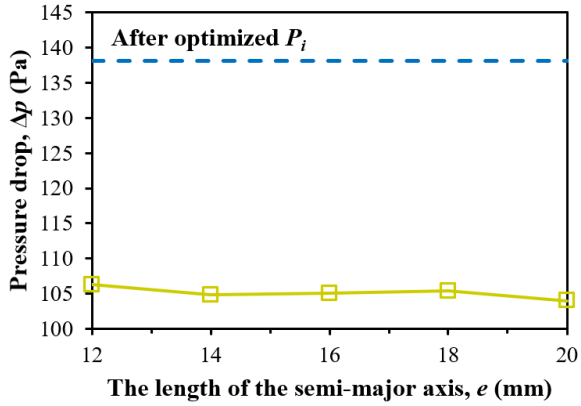

Figure 10

Pressure drop versus the major semi-axis length of elliptical profile, e

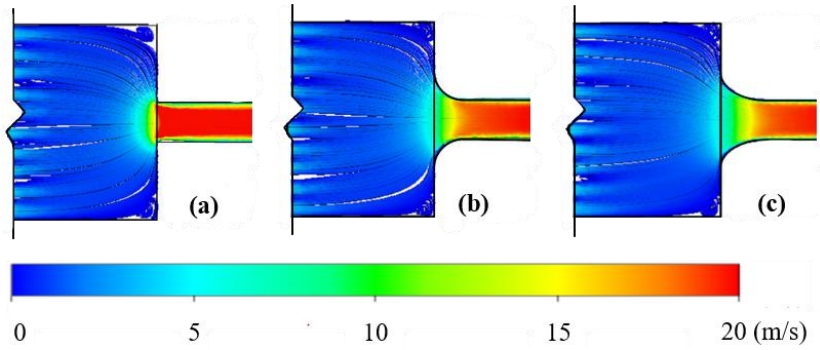

Figure 11

Exhaust flow distribution in the outlet part of the muffler for (a) after optimized Pi, (b) e = 12 mm, (c) e = 20 mm

3.4 Effect of the Polynomial Order of the Contraction Profile, P_o

Figure 12 presents the variation of Δp when exhaust gas passes through the TGS according to the polynomial order of contraction profile, P_o. The results indicate that the fifth-order contraction profile (P_o–5) yields the lowest pressure drop, which is 102.8 Pa. In contrast, the higher-order, seventh (P_o–7) in this case, increases the pressure drop over the previous simulation series. Figure 13 presents the exhaust flow distribution in the outlet part of the muffler after optimizing e, P_o–5, P_o–7. As can be seen in Figures 13a and 13b, the P_o–5 eliminates the vortices in the muffler corner, reducing the pressure drop in this location. However, as the order of the profile increases, it becomes more curved, Therefore, increasing velocity in the outlet part, results in the growth in pressure drop (see Figure 13c). These simulation results indicate that the P_o–5 is the most optimal, confirming what was demonstrated by Bell and Mehta [22].

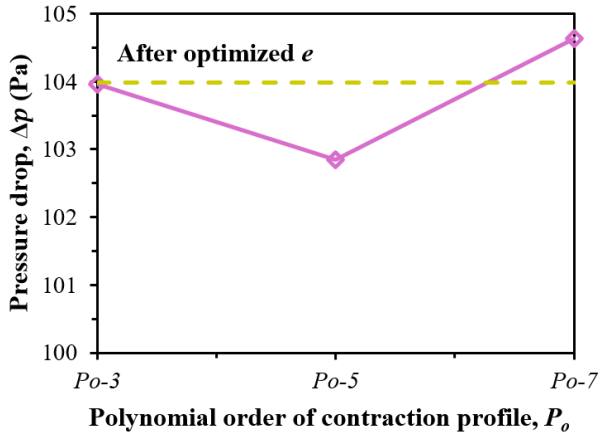

Figure 12
Pressure drop versus the polynomial order of the contraction profile, Po

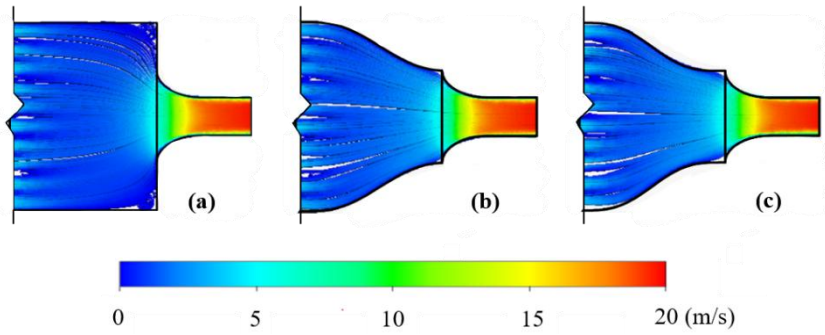

Figure 13

The exhaust flow in the outlet part of the muffler for (a) after optimized e, (b) Po–5, (c) Po–7

3.5 Comparison of Results

Figure 14 presents the pressure drop and pressure power loss of the original model, the optimal model of the previous study, and the optimal model of the present study. It should be noted that the pressure drops of the original and previous optimal models were re-simulated by the new computational model and harvested at the inlet and outlet planes, as described in Section 2.2. After four simulation series, the optimal muffler structure of this work achieves the lowest pressure drop of 102 Pa and power loss due to pressure drop of 0.41 W, representing reductions by 43% compared to the original model and approximately 8% compared to the optimal model of the previous study.

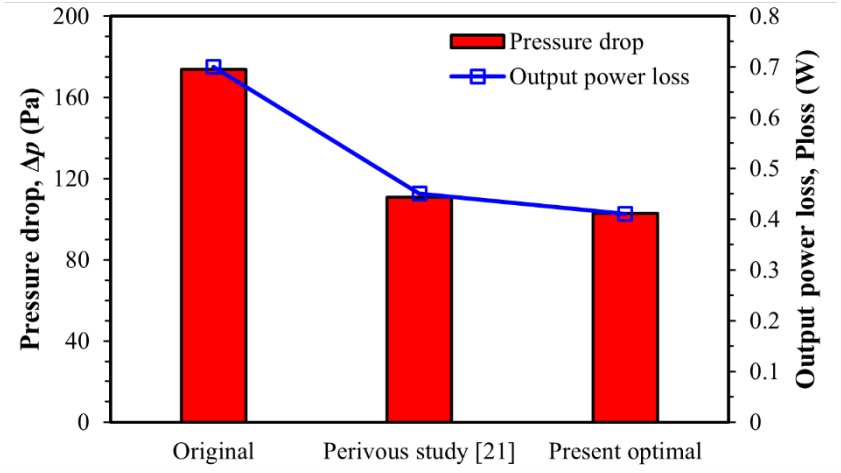

Figure 14

Pressure drop and pressure power loss of the original model, the optimal model of the previous study [21], and the optimal model of the present study.

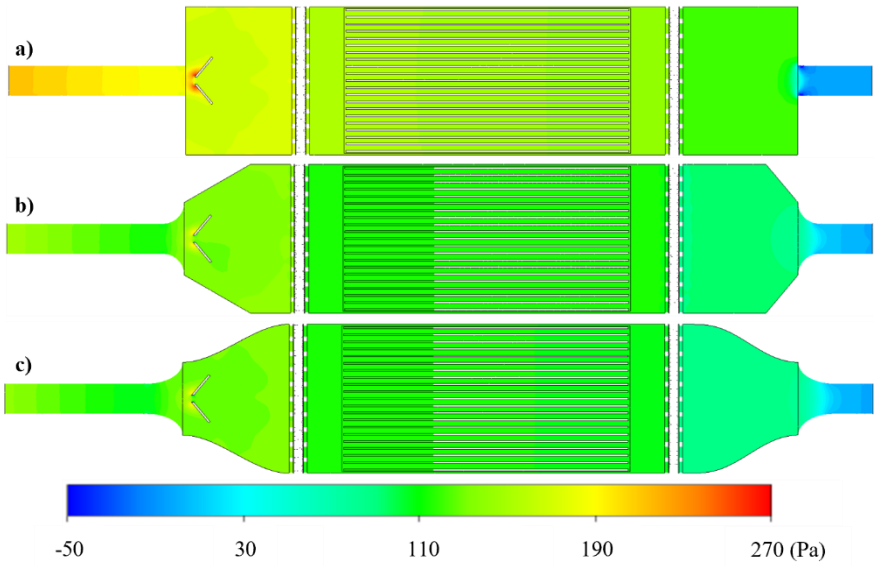

Figure 15
Pressure distribution inside the muffler on the longitudinal section of (a) original model, (b) previous optimal model, (c) present optimal model

Figures 15 and 16 show the exhaust pressure and flow distribution in the muffler for the original, previous, and present optimal models, respectively. Regarding the inlet part, the round and elliptical profiles perform well in limiting sudden flow separation at the junction between the front wall of the muffler and the inlet pipe. In addition, the elliptical profile expands more space in front of the guide fins than the round profile, which slightly reduces the pressure in front of the guide fins. Comparing the chamfer and contraction profiles, the contraction profile more effectively eliminates the vortices in areas bounded by the muffler walls and guide fins; consequently, the pressure drop in the inlet part of the present optimal model is lower than the previous one. Regarding the outlet part, the round and elliptical profiles perform well in eliminating the vena contracta, similar to the inlet part. Moreover, the more gradually varying curvature of the elliptical profile renders the flow distribution more uniform, reducing the local pressure drop. The contraction profile enables a smoother flow transition than the chamfer in the previous model, thereby reducing the pressure drop.

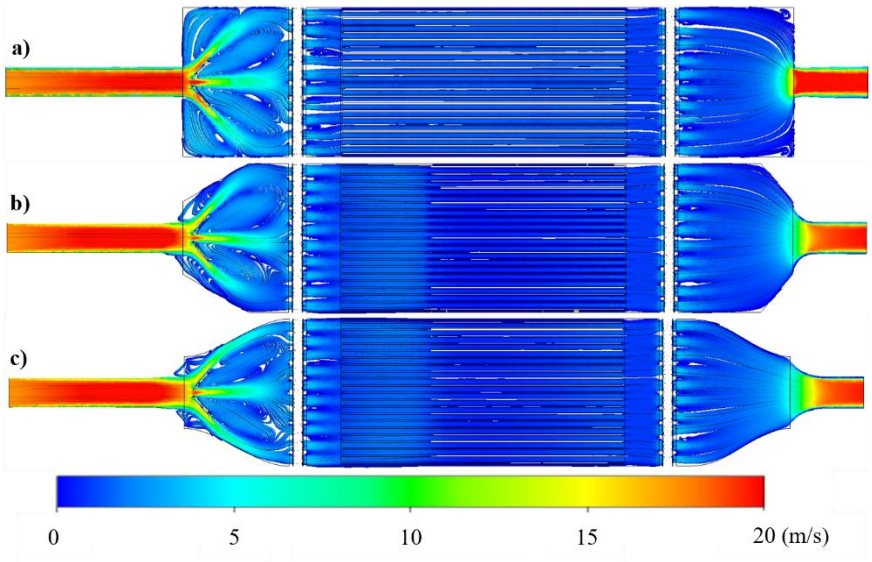

Figure 16
Velocity distribution inside the muffler on the longitudinal section of (a) original model, (b) previous optimal model, (c) present optimal model

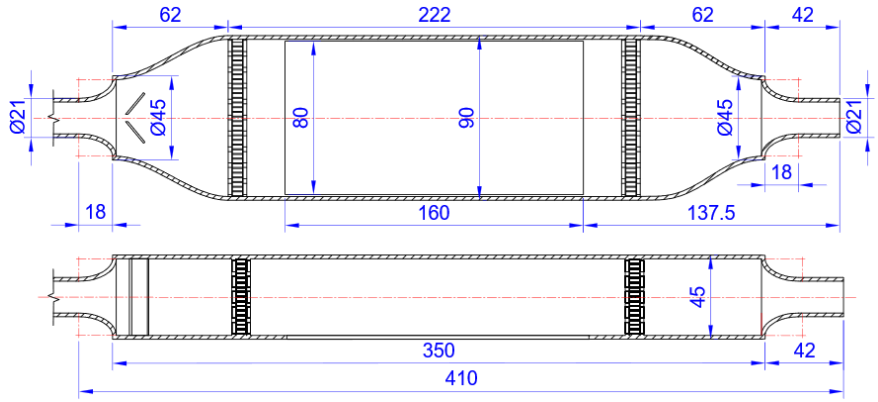

Figure 17
The technical drawing of the optimal muffler configuration

Furthermore, the percentage contributions of the profiles in the optimal model of the present study are calculated by dividing the pressure drop reduction after each optimization series by the total pressure drop reduction of the entire process. The result shows that the contribution of the optimal semi-major axis length b, the polynomial order of the contraction profile P_i, the length of the semi-major axis of the elliptical profile e, and the polynomial order of the contraction profile P_o to the overall pressure drop reduction are 56%, 3.6%, 39%, and 1.4%, respectively.

Finally, the drawing of the muffler with all optimized parameters obtained from the simulation series is shown in Figure 17

Conclusions

In this study, the muffler structure was optimized to minimize pressure drop in a motorcycle exhaust thermoelectric generator by employing high-efficiency aerodynamic profiles. Specifically, the elliptical and contraction profiles were applied in the inlet and outlet of the muffler to reduce local pressure drops, thereby lowering the overall pressure drop of exhaust gas flow. The optimal parameters were analyzed and evaluated through computational fluid dynamics simulations. The principal findings of the study are summarized as follows:

- At the points where the front wall of the muffler connects to the inlet pipe and where the outlet pipe connects to the rear wall, the optimal elliptical profile effectively reduces local pressure drops by eliminating the vena contracta effect. Increasing the semi-major axis at the inlet, b, and the semi-major axis at the outlet, e, further reduced pressure drops, as the transverse area variation along the pipe was decreased.
- At the points between the muffler body and its front and rear walls, the contraction profile effectively eliminates vortices on both the inlet and outlet sides. However, when the polynomial order is excessively high, the profile becomes overly curved, leading to increased pressure drop. On the other hand, applying an elliptical profile with too short a semi-major axis increases pressure drop; meanwhile, when the semi-major axis is adequately long, it mitigates the vortices, thereby reducing pressure. In this case study, the contraction profile outperforms the elliptical profile due to its ability to dissipate vortices in the inlet part.
- The optimal parameters include an elliptical profile at the inlet and front wall, with the semi-major axis b = 20 mm, and a third-order polynomial contraction profile at the junction between the front wall and the body of the muffler. An elliptical profile at the outlet and rear wall, with the semi-major axis e = 20 mm, and a fifth-order polynomial contraction profile between the rear wall and the body of the muffler, provided the lowest pressure drop of 102.8 Pa, reducing by 43% compared to the original design and by 8% compared to the previous study.
- The optimal elliptical profile at the outlet yields the most significant impact, accounting for 56% of the total pressure drop reduction, followed by the outlet elliptical profile with 39%. The contraction profiles at the inlet and outlet parts contribute 3.6% and 1.4%, respectively.

This study contributes to a practical optimal design process for exhaust systems using elliptical and aerodynamic contraction profiles. It serves as an essential reference for practical applications and potential commercialization of

thermoelectric generator systems. Compared with previous research, more complex profiles are employed to achieve improved technical performance; nevertheless, for industrial production, technical, technological, and economic factors must be considered carefully to select the most suitable option.

Acknowledgements

We acknowledge Ho Chi Minh City University of Technology (HCMUT), VNU-HCM for supporting this study.

References

[1] S. N. Hossain and S. Bari: Waste heat recovery from exhaust of a diesel generator set using organic fluids, Procedia Engineering, Vol. 90, pp. 439–444, 2014. https://doi.org/10.1016/j.proeng.2014.11.753

[2] J. Chen, W. Xie, M. Dai, G. Shen, G. Li and Y. Tang: Experiments on waste heat thermoelectric generation for passenger vehicles, Micromachines (Basel), Vol. 13, p. 107, 2022. https://doi.org/10.3390/mi13010107

[3] H. Jouhara, A. Żabnieńska-Góra, N. Khordehgah, Q. Doraghi, L. Ahmad, L. Norman, B. Axcell, L. Wrobel and S. Dai : Thermoelectric generator (TEG) technologies and applications, International Journal of Thermofluids, Vol. 9, p. 100063, 2021. https://doi.org/10.1016/j.ijft.2021.100063

[4] X. Liu, Y. D. Deng, K. Zhang, M. Xu, Y. Xu and C. Su: Experiments and simulations on heat exchangers in thermoelectric generator for automotive application, Applied Thermal Engineering, Vol. 71, pp. 364–370, 2014. https://doi.org/10.1016/j.applthermaleng.2014.07.022

[5] T. D. Hong, Q. T. P. Nghiem, T. V. Mai and L. T. Le: A numerical simulation and experimental study on thermal uniformity of heat exchanger in motorcycle thermoelectric generator unit, JP Journal of Heat and Mass Transfer, Vol. 22, pp. 89–105, 2021. http://dx.doi.org/10.17654/HM022010089

[6] P. Fernández-Yañez, O. Armas, A. Capetillo and S. Martínez-Martínez: Thermal analysis of a thermoelectric generator for light-duty diesel engines, Applied Energy, Vol. 226, pp. 690–702, 2018. https://doi.org/10.1016/j.apenergy.2018.05.114

[7] H. Yang, G. Shu, H. Tian, X. Ma, T. Chen and P. Liu, Optimization of thermoelectric generator (TEG) integrated with three-way catalytic converter (TWC) for harvesting engine's exhaust waste heat, Applied Thermal Engineering, Vol. 144, pp. 628–638, 2018. https://doi.org/10.1016/j.applthermaleng.2018.07.091

[8] T. D. Hong, Q. T. P. Nghiem, T. T. Le, T. M. H. Tran and L. T. Le: Thermal uniformity enhancement of the motorcycle exhaust thermoelectric generator—Part 1: Guide fins optimization, Heat Transfer, Vol. 51, pp. 6177–6196, 2022. https://doi.org/10.1002/htj.22587

[9] T. D. Hong, Q. T. P. Nghiem, B. T. Nguyen and T. V. Mai: Study on the effects of guide fins structures on the flow and thermal uniformity of the motorcycle exhaust thermoelectric generator, Multidiscipline Modeling in Materials and Structures, Vol. 18, pp. 430–444, 2022. https://doi.org/10.1108/MMMS-02-2022-0027

[10] T. H. Hoang, A. T. Hoang and V. S. Vladimirovich: Power generation characteristics of a thermoelectric modules-based power generator assisted by fishbone-shaped fins: Part I – effects of hot inlet gas parameters, Energy Sources, Part A: Recovery, Utilization, and Environmental Effects, Vol. 43, pp. 588–599, 2021. https://doi.org/10.1080/15567036.2019.1630035

[11] T. D. Hong, Q. T. P. Nghiem, P. B. Hua and T. V. Vo: Thermal uniformity enhancement of the motorcycle exhaust thermoelectric generator—Part 2: Muffler outlet optimization, Heat Transfer, Vol. 51, pp. 6470–6488, 2022. https://doi.org/10.1002/htj.22600

[12] R. Attarzadeh, M. Rovira and C. Duwig: Design analysis of the "Schwartz D" based heat exchanger: A numerical study, International Journal of Heat and Mass Transfer, Vol. 177, p. 121415, 2021. https://doi.org/10.1016/j.ijheatmasstransfer.2021.121415

[13] M.A. Zoui, S. Bentouba, D. Velauthapillai, N. Zioui and M. Bourouis: Design and characterization of a novel finned tubular thermoelectric generator for waste heat recovery, Energy, Vol. 253, p. 124083, 2022. https://doi.org/10.1016/j.energy.2022.124083

[14] T. D. Hong, M. Q. Pham and Q. T. P. Nghiem: Thermal uniformity enhancement of the motorcycle exhaust thermoelectric generator—Theory model for predicting heat exchanger fin profile, Results in Engineering Vol. 19, p. 101324, 2023. https://doi.org/10.1016/j.rineng.2023.101324

[15] W. Chen, P. Wu, X. Wang and Y. Lin: Power output and efficiency of a thermoelectric generator under temperature control, Energy Conversion and Management, Vol. 127, pp. 404–415, 2016. https://doi.org/10.1016/j.enconman.2016.09.039

[16] D. Sanin-Villa, O. D. Monsalve-Cifuentes and E. E. Henao-Bravo: Evaluation of Thermoelectric Generators under Mismatching Conditions, Energies (Basel) 14, p. 8016, 2021. https://doi.org/10.3390/en14238016

[17] T. Y. Kim, S. Lee and J. Lee: Fabrication of thermoelectric modules and heat transfer analysis on internal plate fin structures of a thermoelectric generator, Energy Conversion and Management, Vol. 124, pp. 470–479, 2016. https://doi.org/10.1016/j.enconman.2016.07.040

[18] Y. Wang, S. Li, X. Xie, Y. Deng, X. Liu and C. Su: Performance evaluation of an automotive thermoelectric generator with inserted fins or dimpled-surface hot heat exchanger, Applied Energy, Vol. 218, pp. 391–401, 2018. https://doi.org/10.1016/j.apenergy.2018.02.176

[19] T. Y. Kim, J. Kwak and B. Kim: Energy harvesting performance of hexagonal shaped thermoelectric generator for passenger vehicle applications: An experimental approach, Energy Conversion and Management, Vol. 160, pp. 14–21, 2018. https://doi.org/10.1016/j.enconman.2018.01.032

[20] T. D. Hong, M. Q. Pham, K. Q. Huynh and K. Q. Tran: Performance enhancement of the motorcycle exhaust thermoelectric generator - Optimization of the hot-side heat exchanger configuration, Case Studies in Thermal Engineering, Vol. 51, p. 103616, 2023. https://doi.org/10.1016/j.csite.2023.103616

[21] T. D. Hong, K. T. Tran, H. P. Nguyen, M. Q. Pham and A. V. Cao: Optimization Design of Muffler External Geometry Integrated with Motorcycle Exhaust Thermoelectric Generator System, Proceedings of EAI International Conference on Renewable Energy and Sustainable Manufacturing, EAI/Springer Innovations in Communication and Computing, Ho Chi Minh City, 2024, pp. 563–581. https://doi.org/10.1007/978-3-031-60154-5_36

[22] B. H. James Bell and R. D. Mehta: Contraction design for small low-speed wind tunnels, NASA Technical Reports Server, 1988, https://ntrs.nasa.gov/citations/19890004382 (Accessed: May 05, 2024)

[23] M. Liu, C. Jiang, B. C. Khoo, H. Zhu and G. Gao: A cell-based smoothed finite element model for the analysis of turbulent flow using realizable k-ε model and mixed meshes, Journal of Computational Physics, Vol. 501, p. 112783, 2024. https://doi.org/10.1016/j.jcp.2024.112783

[24] H. Yan, Y. Liu, Q. Li and L. Lu: Turbulence characteristics in corner separation in a highly loaded linear compressor cascade, Aerospace Science and Technology, Vol. 75, pp. 139–154, 2018. https://doi.org/10.1016/j.ast.2018.01.015

[25] R. Li, L. Gao, C. Ma, S. Lin and L. Zhao: Corner separation dynamics in a high-speed compressor cascade based on detached-eddy simulation, Aerospace Science and Technology, Vol. 99, p. 105730, 2020. https://doi.org/10.1016/j.ast.2020.105730

[26] Y. Nakayama and R. F. Boucher: Introduction to fluid mechanics, Butterworth-Heinemann, Oxford, 1998. https://doi.org/10.1016/B978-0-340-67649-3.X5000-3